Astronomy & Astrophysics manuscript no. main
October 20, 2021

Characterising coronal turbulence using snapshot imaging of radio bursts in 80 – 200 MHz

A. Mohan

Rosseland Centre for Solar Physics, University of Oslo, Postboks 1029 Blindern, N-0315 Oslo, Norway
Institute of Theoretical Astrophysics, University of Oslo, Postboks 1029 Blindern, N-0315 Oslo, Norway
e-mail: atulm@astro.uio.no

Received - 27 Aug 2021 ; Accepted - 10 Oct 2021

ABSTRACT

Context. Metrewave solar type-III radio bursts offer a unique means to study the properties of turbulence across the coronal heights. Theoretical models have shown that the apparent intensity and size of the burst sources evolve at sub-second scales under the influence of local turbulence. The properties of the evolution varies with frequency. However, observational studies remained difficult due to the lack of high fidelity imaging capabilities at these fine temporal scales simultaneously across wide spectral bands.
Aims. I present a spectroscopic snapshot imaging (0.5 s, 160 kHz resolution) study of a type-III burst event across 80 – 200 MHz band. By modelling the temporal variability of the source sizes and intensity at every observation frequency, the characteristics of coronal turbulence is studied across a heliocentric height range of $\approx$ 1.54 – 1.75 $R_\odot$.
Methods. To understand the morphological evolution of the type-III source, a 2D Gaussian fitting procedure is used. The observed trends in the source area and integrated flux density are analysed in the framework of theoretical and data driven models.
Results. The strength of density fluctuations (δN/N) in the corona is derived as a function of height (R). Combined with the archival low frequency data, δN/N values across $\approx$ 1.5 – 2.2$R_\odot$ agree within a few factors. The burst decay time (τ_{decay}) and the FWHM of the source showed a power-law dependency with frequency, roughly consistent with the results from data driven models. However, the values of τ_{decay} across frequency turned out higher than the expected trend. The intrinsic sizes of the burst source were derived correcting for scatter broadening. This roughly matched the expected size of flux tubes at the coronal heights explored. I also report the observation of an intrinsic anti-phased pulsation in area and flux density of the source.

Key words. giant planet formation – κ-mechanism – stability of gas spheres

1. Introduction

Type-III bursts are triggered by supra-thermal electron beams produced at various particle acceleration sites in the solar corona, especially at active regions (Wild 1950). These particle beams move along nearby open magnetic field structures tracing a range of coronal heights, generating two-stream instability along the trajectory. Langmuir wave turbulence generated by the instability triggers various wave-wave and wave-particle interactions leading to coherent plasma radiation from the regions along the beam trajectory at the respective local plasma frequencies (ν_p) and its harmonics ($2\nu_p$) (e.g., Ginzburg & Zhelezniakov 1958; Tsytovich & Kaplan 1969; Melrose & Sy 1972). However, the observed emission is heavily influenced by the stochastic density fluctuations in the medium, primarily owing to the fact that the frequency of the radiation (ν) is close to the local ν_p.

The plasma frequency is a function of local density (N) and the local refractive index (n) is a strong function of ν_p/ν,

$$\nu_p = \left[8980\left(\frac{N}{1 cm^{-3}}\right)^{0.5}\right] MHz, \quad (1)$$

$$n = \sqrt{1-(\nu_p^2/\nu^2)}. \quad (2)$$

So the turbulent fluctuations in the local density (N) causes stochastic fluctuations in the local refractive index which causes the waves to undergo multiple random scatterings across the medium until they propagate to a height beyond which the mean refractive index, $\bar{n}$, is close to 1. Several works have studied the wave propagation effects in corona using Monte-Carlo simulations (e.g, Steinberg et al. 1971; Robinson 1983). A detailed analytical formalism for the radio-wave propagation was developed by Arzner & Magun (1999) (AM hereafter). Their work provided a set of analytical equations to model the observed temporal profiles of the burst source properties like intensity, size and mean drift in the image plane. AM predicted that the source sizes and intensity would follow a trend of initial rise leading to a maximum value and a subsequent decay. The analytical expressions for these trends encapsulate the basic features of the local coronal turbulence like density fluctuation index (δN/N), width of the strong scattering region etc. However, to apply this model to data and make reliable estimates of the properties of coronal turbulence, sub-second scale imaging capability with sufficient imaging fidelity is required. The modern interferometric arrays like the Murchison Widefield Array (MWA, Tingay et al. (2013); Wayth et al. (2018)), LOw Frequency ARray (LOFAR, van Haarlem et al. (2013)) etc. have facilitated such studies.

Using LOFAR observations of a type-III burst, Kontar et al. (2017) demonstrated the trend predicted by AM in the source sizes in tandem with intensity and highlighted the relevance of scattering effects in observed burst sources. Mohan et al. (2019) presented the temporal evolution profiles for a type-III source associated with a microflare at 0.5 s resolution observed at various observation frequencies across a 15 MHz band centred at 118 MHz. The authors modelled the initial rise phase of the

source size evolution and derived the δN/N within the coronal height range sampled by the 15 MHz band, during the event. Meanwhile, extension of the framework by AM was recently carried out by Kontar et al. (2019) (K19 hereafter), who also compared the theoretical model with archival observations. The authors presented a detailed simulation framework also to model the wave propagation through both isotropic and anisotropic scattering medium. The authors derived power-law functions for the burst source sizes and intensity decay times as a function of frequency using empirical fits to archival data. In a recent work, using simulations based on K19 framework Zhang et al. (2021) performed parametric simulation studies by varying the level of anisotropy and δN/N in the scattering medium to predict the position offset, size and duration of the radio burst sources seen at 35 MHz.

However, there has not been much works that observed and modelled the co-evolution of source morphology and intensity during bursts at sub-second cadence to derive the characteristic parameters of local coronal turbulence like δN/N, size of the scattering screen etc. The study by Mohan et al. (2019), which was one such study explored only a small bandwidth of 15 MHz that corresponded only to a very small height range of about ten times smaller than the local density scale height, as mentioned by the authors themselves. The current work aims to perform a similar, but more detailed, analysis across a much larger height range using data taken across a wide spectral band from 80 – 240 MHz during another type-III event. A data across such a wide spectral sampling will help understand the nature of coronal turbulence and its impacts on radio wave propagation across a broad range of heights in the corona.

Section 2 will present the details of the solar event and the observations, followed by analysis in Sec. 3. A discussion on the inferences from the analysis will be presented in Sec. 4 followed by conclusions.

2. Observations

Archival MWA Phase-I data are used for this work. A search for type-III events observed by MWA in the "picket fence" observation mode was done. In picket fence mode MWA observes the sun simultaneously within 12 spectral bands of width 2.56 MHz, sparsely distributed across the operational bandwidth of 80 – 240 MHz. Of the type-III observations carried out in picket fence mode, the burst source which satisfy two criteria were shortlisted.

1. Burst region is close to disk centre.
2. No possible flux contamination from transient or persistent bright nearby sources.
3. Temporally separable burst pulses.

The first criteria lets us safely assume an isotropic scattering model. This is because of the following reason. The coronal open magnetic field structures, along which the type-III initiating supra-thermal electrons travel are mostly aligned radially. Choosing a disk-centre source ensures the alignment of line of sight and the radial vector. The characteristics of the turbulence power spectrum along the axes perpendicular to the radial vector can typically be assumed to be similar.This lets us assume isotropic scattering in the plane perpendicular to radial vector, i.e. the image plane for a disk-centre source. But if we chose sources close to limb, the radial vector is no more oriented along line of sight and the shape of the source becomes asymmetric subject to strong anisotropic scattering effects in the image plane (Refer, AM & K19), subject to different spatial scales of scattering along and across the magnetic field structures. These different scales increase the degree of freedom in the problem and making source evolution modelling harder. The analytical equations get simpler for the isotropic case and are readily available in AM (and K19). Modelling is also less ambiguous in the isotropic case since one need not worry about the unknown characteristic length scales of open magnetic field structures, but can use the typical generic scattering scales in the corona (e.g. Coles & Harmon 1989; Sasikumar Raja et al. 2017). The second criteria ensures that the observed the radio source evolution is attributed solely to propagation of radio emission from the compact type-III burst alone and not contaminated by any sources nearby the burst location. The cases where a pre-existing persistent source was present near or at the burst location were also excluded from the study. The third criteria directs the search to observations of bursts with pulse like temporal profiles. Usually in observations of type-III bursts, multiple strokes of bright burst emission can be seen in the dynamic spectra, caused by pulsed particle acceleration/injection (e.g. Aschwanden et al. 1994; Wang et al. 2003; Mohan et al. 2019). It is seen in several cases that the time gap between these pulsed acceleration episodes are smaller than the time-scale of scatter broadening of pulse profiles making them merge and hard to separate, especially seen in low frequency observations. In such cases, the scatter broadened source shapes seen in image plane and the intensity profiles seen in dynamic spectra from multiple would merge, making the individual study of each burst episode hard. This makes the study of the effect of scattering/local turbulence on a single burst pulse/episode difficult. So, by applying these selection criteria on MWA-phase-I observational database, I plan to identify the type-III events involving burst episodes well separable in the dynamic spectral plane and produced by disk-centred sources distinguishable in the image plane throughout the event. These sources will help perform an unambiguous study of the response of the local corona to the individual burst pulses at sub-second scales across the coronal heights probed by the wide MWA band.

A search based on the above criteria, found one dataset from 2015-11-11, 02:29:00 – 02:34:00 UT as the only appropriate match for this work. The observations had a spectro-temporal resolution of 40 kHz and 0.5 s. The few other on-disk type-III events when imaged, were found to not satisfy the second and third criteria. The event presented here, was among the type-III events studied by Rahman et al. (2019) using archival MWA Phase-I data, where the authors explored the evolution of the degree of polarisation, source motion and intensity decay time as a function of frequency. Source size evolution, crucial to understand the propagation of radio waves, was not covered in that work. Also the authors used full sun dynamic spectrum for their studies. In this study we will use spatially resolved dynamic spectra with detailed source structure modelling across the entire frequency and time range of the observations.

3. Analysis

Data downloaded from the MWA repository was imaged using AIRCARS calibration and imaging pipeline Mondal et al. (2018). The absolute calibration of the fluxes are not performed since this is not important for the scientific goals of his study. So the final images are in arbitrary flux units. Of the 12 observational bands, the two highest frequency bands had to be discarded owing to bad data quality. So, the final spectral coverage achieved is 80 – 200 MHz. The burst event started at

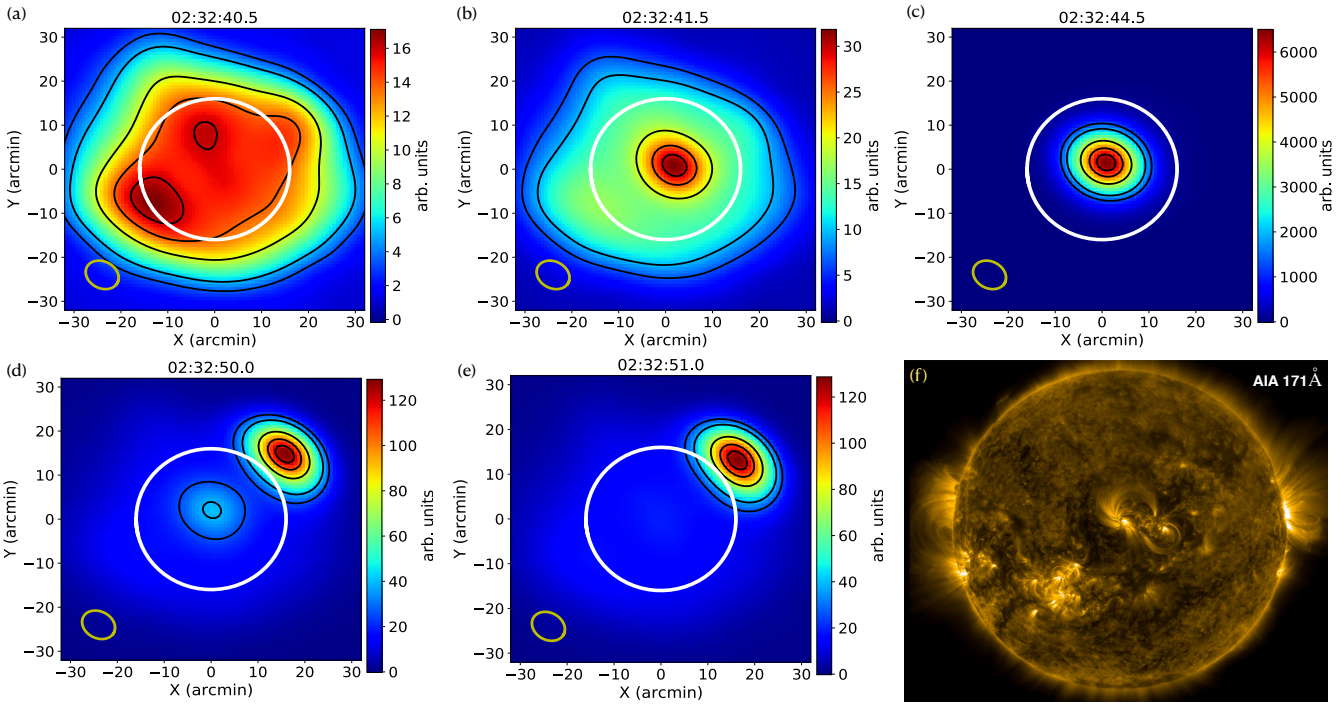

Fig. 1. (a–e): 109 MHz images during different times: (a) just before the start, (b) at the start, (c) at the peak, (d) towards the end, and (e) after the end of the burst. The images are at the same arbitrary unit scale. Image contours: 20, 30, 60, 80 & 93% of the peak. The synthesised beam ellipse is shown in the bottom left corner of the images. White circle marks the optical disk. (f): AIA 171Å image at 02:32:00 UT, showing a bright active region at the disk centre during the burst.

different times, within 02:32:41.0 – 02:32:50.5 UT, in different bands. Figure 1 (a – e) show the images of the Sun at the mid-frequency of the operational band, during different phases of the burst. The burst source that appeared transiently at the disk centre had a 2D Gaussian morphology with no pre-existing sources or nearby bright events before, during or after the event. The type-III source of interest is possibly related to the active region near the disk centre evident in the AIA 171Å image shown in Fig. 1(f).

3.1. SPatially REsolved Dynamic Spectrum (SPREDS)

The bursts source across all frequency and time of observation, had a 2D Gaussian morphology. To understand the complete spectro-temporal evolution of the burst source, the images across all spectral bands of observation during the entire duration of the event were modelled using the imfit routine in the Common Astronomy Software Applications (CASA; McMullin et al. 2007) software. Each burst image was modelled as a linear combination of a 2D Gaussian function and a constant offset. The offset accounted for the background emission. The parameters of the 2D Gaussian model returned by imfit included the integrated flux density, the peak flux density, the source location and the Full Width at Half Maximum of the major and minor axes of the source after deconvolving the effect of the synthesised beam ($\mathrm{FWHM}_{\mathrm{maj(min)}}$). Using $\mathrm{FWHM}_{\mathrm{maj(min)}}$, the standard deviations of the Gaussian source were computed ($\sigma_{\mathrm{maj(min)}}$) and its area in the image plane was estimated as $\pi\sigma_{\mathrm{maj}}\sigma_{\mathrm{min}}$. This definition of area makes it easier to compare the observations with the analytical expressions derived by AM. SPatially REsoled Dynamic Spectrum (SPREDS), originally defined for flux density measurements of the source region as a function of time and frequency (Mohan & Oberoi 2017) is now extended to other properties of the burst source as well. Figure 2 shows the SPREDS for integrated flux density, area, σ_{maj} and σ_{min}. The burst happens first in high frequency bands and progresses to lower bands, hinting at a beam of high energy electrons streaming outward into the corona (See Reid & Ratcliffe 2014). Interestingly, the evolution in σ_{maj} and σ_{min} are quite similar qualitatively and quantitatively. This supports the practicality of the assumption of isotropic scattering in the image plane. Note that the images in the high frequency bands suffered from poor quality and hence gave no reliable Gaussian fits during the start time of the burst, resulting in the lack of SPREDS data.

Another interesting feature is the systematic delay of a few seconds in the peaking of the source area with respect to its integrated flux density. To make this effect more clear, Fig. 3(a) shows the mid-band time profiles for area and integrated flux density for each of the 10 picket fence spectral bands. The time profiles are normalised by the respective maximum values for the ease of presentation without distortion/loss of relevant information. The integrated flux density and the area evolution showed pulse profiles in all frequencies except in the two high frequency channels, which suffered from relatively poor imaging quality. The pulse profiles in the two source properties appear shifted in time domain. Figure 3(b) shows the normalised cross correlation (NCC) analysis done on the two property evolution profiles to robustly estimate this delay in the peaking. I report a delay of $\approx 2 - 3$ s. NCC also shows an anti-correlation signature around a time lag of $\approx 0 - 1$ s. This however is not a strong signature, like the correlation around 2 s, across all the bands where burst pulses are detected. A closer look at the type-III events presented by Kontar et al. (2017) and Mohan et al. (2019) also reveal time delays in the peaking of the area and integrated flux density profiles of the same order. Apart from this, the flux density pulses

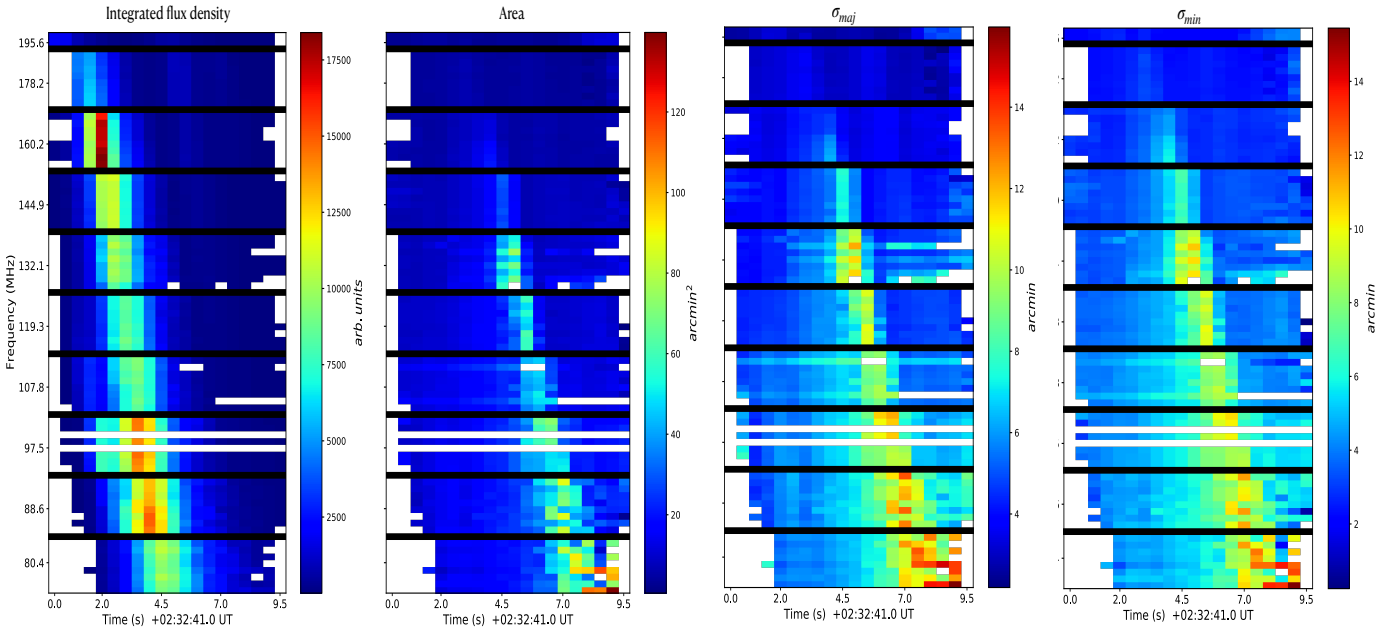

Fig. 2. SPREDS for different burst source properties. The black horizontal lines mark the edges of the spectral bands. White regions are masked due to bad data (usually in frequencies above 140 MHz) or due to the absence of a bright Gaussian burst source.

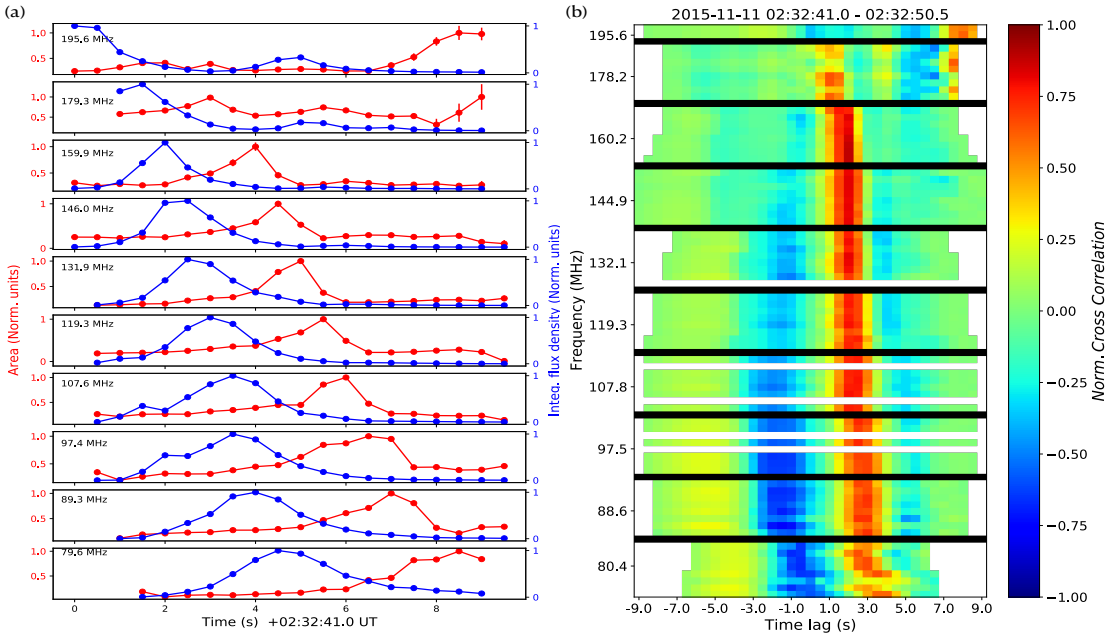

Fig. 3. (a):Light curves for area and integrated flux density evolution at the mid-frequencies in each spectral band. Each light curve is normalised by the respective maximum value. (b): NCC analysis for area and integrated flux density.

(hereafter, "burst pulses") tend to broaden as the observation frequency decreases.

4. Discussion

It is clear from Fig. 2, that the temporal profiles of different source properties are quite similar across the 2.56 MHz wide spectral bands. The NCC analysis shown in Fig. 3 also testifies to this. Physically this is expected since 2.56 MHz bandwidth when converted to coronal height range will correspond to less than 5% of the pressure scale height and density variation scale (N[dN/dR]$^{-1}$) assuming any typical coronal density model widely used. So the mean properties of the medium explored within this bandwidth are expected to remain similar. Hence, for further analysis, I choose a light curve from every 2.56 MHz band, such that the number of masked data points in the time domain are less and the observation frequency falls roughly close to the band centre. Fig. 3a shows these chosen light curves in every band with the corresponding observation frequency labelled. Of these chosen property evolution profiles, we further restrict the analysis to the frequencies below 170 MHz. This is because the sampling of the burst pulse is poor in the frequencies above 170 MHz and the objective of the work is to understand the co-

evolution of the area and flux density of the burst from the start of the type-III pulse.

To progress further, the observed burst emission is assumed to be produced at the harmonic of the local plasma frequency. This assumption is backed by two facts. Firstly, since the fundamental emission is known to be heavily affected by scattering and other propagation effects (e.g. Steinberg et al. 1971; Robinson & Cairns 1994; Robinson 1983), if only one branch/stroke of type-III bursts are observed in the meterwave flux dynamic spectrum, it is most likely to be harmonic emission (Reid & Ratcliffe 2014). Secondly, the degree of circular polarisation (p) of the observed bursts were found to be within $\approx 10 - 30\%$, with a mean around 20%, by Rahman et al. (2019). This range of values and the mean is below the expected range of $p > 30\%$ and mean of $p \approx 35\%$ for the fundamental emission component (Dulk et al. 1984). So, using the assumption of harmonic emission, the observation frequencies were converted to densities at the burst site using Eqn. 2. Later, using a recent coronal density model by Alcock (2018),

$$N(R) = 4.8 \times 10^9 \left(\frac{R_\odot}{R}\right)^{14} + 3 \times 10^8 \left(\frac{R_\odot}{R}\right)^{6} + 1.4 \times 10^6 \left(\frac{R_\odot}{R}\right)^{2.3}. \quad (3)$$

the heliocentric height of the burst site (R) in the corona was discerned for each observation frequency. With density and heights estimated, the apparent source properties at each observation frequency can now be modelled to derive the stochastic properties of the corona and the intrinsic burst source dynamics across height.

4.1. Effects of scattering in the source evolution

According to the model for the propagation of radiowaves by AM, the wave with frequency, $\nu < \nu_p$, undergo multiple refractions at randomly distributed sites of local over and under densities as it propagates outward to the observer. This causes the otherwise impulsive narrow time profile of the burst pulse to appear broadened and the apparent source size in the image plane to grow with time. The effect of scattering in wave propagation is high when the local refractive index, n, of the wave is considerably less than unity (AM & K19). Due to the relatively lower n at the generation site, the effect of scattering is more prominent and lasts for a larger extent of the propagation distance for the fundamental emission compared to the harmonic. As mentioned in Sec. 1, modern interferometric arrays have facilitated the tracking of sub-second evolution of the apparent radio burst source structure, subject to radiowave propagation effects across the corona. These observations let us now model the propagation effects using existing theoretical framework and derive the characteristics of coronal turbulence.

AM derived equations relating the scatter broadened burst intensity and the source area evolution profiles (See, Eqns.62 – 65). In the case of strong scattering, AM predicted a linear growth in the observed source area until it reaches a saturation value, which is a function of the strength of density fluctuations, $\delta N/N$ in the medium. Meanwhile, the growth rate, D_s is a function of the isotropic ray diffusion coefficient η^*, which in turn depends on $\delta N/N$, the mean inverse spatial ($|\mathbf{k}|$) scale ($<\kappa>$) and the spatial profiles of plasma frequency, ν_p and the refractive index, n in the medium. The flux density rise time of the burst pulse, <t>, also depends on η^* and $\bar{n}$ during strong scattering. The authors also defined a "strong turbulence" regime for the scattering medium, during when the $\delta N/N$ in the medium is greater than a theoretical saturation threshold $\delta N/N_{sat}$. $\delta N/N_{sat}$ depends only on the basic properties of the scattering medium namely $\bar{n}$ and its thickness (L). If a scattering medium is in this regime, the saturation value of the apparent source area for an intrinsically point burst source becomes practically independent of $\delta N/N$ variation in the medium and it asymptotes to a constant ($\pi {\sigma_{sat}}^2$) dependent only on the thickness of the scattering medium. For an intrinsically extended burst source this saturation area gives the scale of scatter broadening, because the effect of the scattering screen on a source is that of a convolution filter. Equations 4 – 8 presents the equations valid for strong scattering derived by AM (Also used in Mohan et al. 2019).

$$D_s = \frac{\pi(c\bar{n})^2}{3\eta^* D^2} \quad (4)$$

$$< t > = \eta^* \left(\frac{L}{c\bar{n}}\right)^2 \quad (5)$$

$$\eta^* = \frac{\pi}{8}\frac{c}{\nu^4} < \kappa > \frac{\overline{\nu_p^4}}{n^3}\left(\frac{\delta N}{N}\right)^2 \quad (6)$$

$$\sigma_{sat} = \frac{L}{\sqrt{3}D}. \quad (7)$$

$$\frac{\delta N}{N}_{sat} = 1.5\frac{\bar{n}^2}{1-\bar{n}^2}\left(\frac{l_i}{L}\right)^2 \quad (8)$$

In the above equations, c is the speed of light, D is the Earth-Sun distance and l_i is the inner scale length of turbulence. $\overline{\nu_p^4/n^3}$ represents the mean of ν_p^4/n^3 across the thickness of the scattering screen. The mean density is expected to vary radially outwards across the scattering medium. So, ν_p and thereby n, also varies across the scattering medium as the radiowaves propagate outwards. Note that since $n \approx 0.86$ at the site of generation of the harmonic emission, even a 30% drop in local density will decrease the effect of scattering significantly as n becomes greater than 0.92. So the size of the effective scattering screen, L, for the harmonic emission tends to be smaller than the typical local pressure scale height. This was demonstrated in a type-III dataset around 111 MHz by Mohan et al. (2019) (Refer Sec. 4.1.1). Hence, the characteristic properties of the medium namely, $\delta N/N$, $<\kappa>$ and l_i are assumed to be constant across the scattering medium.

A closer inspection of the area evolution during the period spanning the rise to decay up to half the maximum value of the burst pulse profile, revealed that the area evolution is well defined by a linear growth model (Fig. 3(a); See Sec. 4.1.1 for details). Such a correlated growth in burst sizes and intensity is expected to result from strong radiowave scattering effects in the corona. This behaviour can be noted in the data presented by Kontar et al. (2017) and Mohan et al. (2019) as well. Meanwhile, in the declining phase of the flux density, a more rapid rise in area followed by a dramatic decline, resembling a pulse profile, is seen. This resulted in the strong correlation signal seen in the NCC analysis (Fig. 3(b)) at a lag of $\approx 2 - 3$ s across all spectral channels with a good sampling of the burst pulse. Though an anti-correlation at zero time lag is also found in the NCC plots in some some bands, it is noteworthy that this feature is not present in all picket fence bands. This is because the area evolution shows a linear growth during the rise of the flux density pulse until its initial declining phase. At higher spectral bands where the scatter broadening effect is smaller, it becomes more clear that the area pulse and the area rise are distinct events. A post-burst pulsed evolution in area is not expected from the ra-

diowave propagation models by AM or K19, where the effect of scatter broadening in both area and flux density should happen simultaneously. So, this pulsation in area could be due to a true variation in the cross section of the accelerated electron beams that caused the type-III bursts. Such time-lagged pulsations in area and integrated flux density at similar delay time scales have been reported in the metric type-III bursts by Mohan et al. (2019). This is believed to be caused by the coupling of sausage-like MHD modes to the sites of generation of accelerated particle beams which trigger the type-III bursts, as proposed by certain earlier works (e.g. Rosenberg 1970; Aschwanden et al. 2004) based on dynamic spectral studies. Recently this phenomenon was reported in solar type-I noise storms as well (Mohan 2021; Mondal & Oberoi 2021).

Since the observed area evolution trends during the type-III burst pulse phase follows a linear trend, characteristic of strong scattering, the equations 4 – 8 are applicable. From the linear area growth rate (D_s) during the burst pulse, and the flux density rise time (<t>), the width of the effective scattering layer (L) across the heights probed by various observation frequencies can be found. Assuming the density profile, N(R), the mean refractive index,$\bar{n}$ and $\overline{\nu_p^4/n^3}$ across L can be computed. The estimation of δN/N, however requires the knowledge of the mean inverse scale length of turbulence/scattering in the medium, $<\kappa>$. Assuming Kolmogorov turbulence, expression for $<\kappa>$ takes the following form (AM & K19),

$$<\kappa> = 2\frac{{\kappa_o}^{1/3} - {\kappa_i}^{1/3}}{{\kappa_o}^{-2/3} - {\kappa_i}^{-2/3}}, \quad (9)$$

where κ_i and κ_o are the inner and outer inverse spatial ('k') scales of turbulence in the scattering medium. These k-scales are linked to spatial scales as,

$$\kappa_i = 2\pi/l_o \quad (10)$$
$$\kappa_o = 2\pi/l_i \quad (11)$$

where l_i and l_o are the inner and outer spatial scales of turbulence. The value of l_i is assumed to be three times the local ion inertial scale, based on previous observational results (Coles & Harmon 1989; Sasikumar Raja et al. 2017). To get an estimate for l_o, the prescription by Wohlmuth et al. (2001) is used.

$$l_i = \left[684\left(\frac{N}{1 cm^{-3}}\right)^{-0.5}\right] km, \quad (12)$$
$$l_o = \left[0.25(R/R_\odot)^{0.82}\right] R_\odot, \quad (13)$$

where R is the heliocentric height of the radio burst source and N is the local density. For a case where $L << l_o$, κ_i can be practically assumed to be 0. This simplifies Eqn. 9, which when recast using Eqn. 11, takes the form,

$$<\kappa> = 4\pi/l_i \quad (14)$$

The values of the different spatial scales (L, l_o and l_i) can thus significantly modify the expression of the mean k-scale ($<\kappa>$). This in-turn alters of the final expression for η^*, which links the observables to δN/N. So it is important to get reliable estimates for the various spatial scales.

4.1.1. The estimation of the spatial scales

The inner (l_i) and outer (l_o) scales of turbulence were computed for the observation frequencies by substituting the corresponding N and R estimates in Eqn. 12 & 13. L was estimated as a function of R, using the values for D_s and <t> for the respective observation frequencies as mentioned in the previous section. D_s was found by fitting a linear function to the area evolution during the flux density pulse period for observation frequencies below 179 MHz where the pulse profile is evident in the flux density light curve. The χ^2-fitting procedure to deduce D_s, succeeded with errors less than ≈5% for the area evolution curves at all chosen frequencies except at 159.9 and 146 MHz. At these two highest of the chosen frequencies, it was found that the area was practically constant during the burst. This could be because the area growth phase was too rapid to be sampled with the time resolution of 0.5 s. This effect is expected as we probe at high frequencies. This is because the higher frequencies probe denser and deeper layers of the corona, where the density gradients are higher. Since the effective scattering screen can be envisaged as the region within which the refractive index is considerably less than 1, a steeper local gradient in n leads to smaller scattering screen width, L. Thinner screens lead to shorter radiowave propagation timescales across them, resulting in faster area growth rates. Since, the system is under strong scattering regime, the observed mean area at these frequencies could be the saturation area, σ_{sat}, predicted by AM. A corollary to this effect is that the observed burst flux and area pulse profile in frequencies above 146 MHz should be reflecting a true intrinsic variation since the effect of scatter broadening is already saturated. This supports the suggested scenario of sausage-mode like intrinsic dynamics at the particle acceleration/injection site resulting in the time-delayed correlated area-intensity pulsation. At lower frequency bands, this intrinsic effect is modified by scattering to a larger extent as is evidenced by the clear initial linear growth of area.

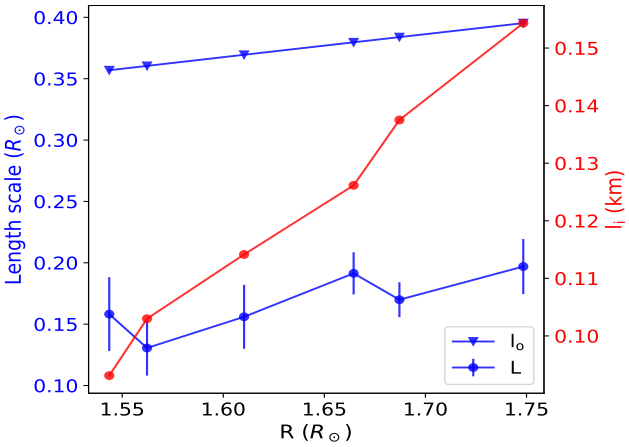

Fig. 4. The different scale lengths L, l_i and l_o Vs R.

Fig. 4 shows the different length scales as a function of heliocentric source heights as derived from the area evolution profiles at the chosen frequencies below 146 MHz. Note that the scale used for l_i is in km while l_o and L are in $R_\odot$, to make the trend in l_i evident. The L values are much less than l_o, which makes Eqn. 14 a good approximation. Also, L decreases with decreasing R or increasing observation frequencies as expected.

4.1.2. Estimating δN/N

With the estimates for L and N across R, $\bar{n}$ and $\overline{\nu_p^4/n^3}$ were computed. η^*(R) was found using Eqn. 4, . With $<\kappa>$(R) known, by rearranging Eqn. 6, δN/N(R) was obtained. δN/N_{sat} was also estimated using Eqn. 8 to know the regime of turbulence – strong or weak, as mentioned in Sec. 4.1. Fig. 5 shows the δN/N(R)

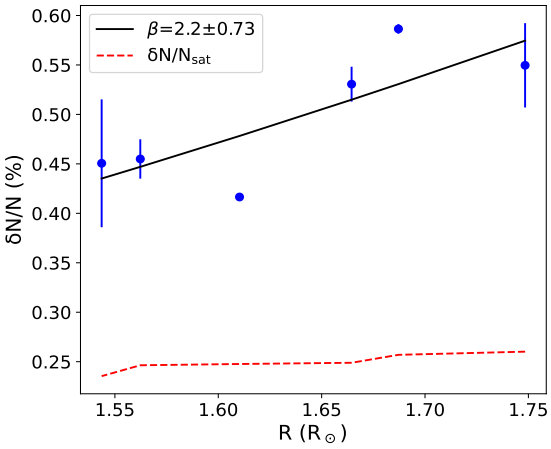

Fig. 5. δN/N and δN/N_{sat} as a function of R. A power-law fit to δN/N is shown in solid line.

and δN/N_{sat}(R). δN/N values range within 0.42 – 0.6 %, with a hint of a rising strength of density fluctuations with height. A power-law fit assuming $\delta N/N \propto r^{\beta}$ gave an index, $\beta = 2.2 \pm 0.73$. δN/N_{sat} being greater than δN/N, the system under study is in strong turbulence regime. So the scatter broadening effect is expected to be saturated at a value of σ_{sat}, despite the case of even large variations in δN/N. This lets us estimate the true intrinsic size of type-III sources by deconvolving the scatter broadening area scales (σ_{sat}) from the observed areas across R.

4.1.3. Goodness of the assumptions on the mean stochastic properties

The framework employed here assumed that the mean properties of turbulence namely δN/N, l_i and l_o, in the medium is fairly uniform across the scattering screen width, L. Note that the strength of $\eta*$ can vary within the scattering screen and it is the variable that reduces the effect of scattering on radio waves as they propagate outward across L.

Figure 4 shows that L $\approx$ 0.15 $R_\odot$within $\approx$ 1.52 – 1.67 $R_\odot$. It slowly rises to $\approx$ 0.2 beyond 1.7 $R_\odot$. Within the height scale of 0.15 – 0.2, the l_i values changes only by <10% and $l_o \approx 5\%$. Similarly, δN/N is constant within error bars in 1.52 – 1.67 $R_\odot$ and in 1.67 – 1.75 $R_\odot$ ranges. Using the derived best-fit model of δN/N, the variational scale of δN/N, i.e., $[\delta N/N]/[d\delta N/N/dR] \approx$ R/2.2. This scale is $\approx 0.7 R_\odot$ at 1.575 and $\approx 0.8 R_\odot$ at 1.7, which are much higher than L. These analyses show that the assumption of uniform stochastic properties within the scattering screen is fairly good and the derived δN/N estimates are reliable.

Another assumption inherent in this model is that the effect of propagation is primarily restricted to within the scattering screen. This is a fair assumption since the scattering is primarily due to the refractive index fluctuations (δn) induced by the density inhomogenieties in the medium and the ratio of δn to mean local refractive index, $\bar{n}(R)$, is very low outside the scattering screen of width L. The emission being at the harmonic of local ν_p, $\bar{n}$ is already $\sim$ 0.86 at the generation site. By the time it crosses the scattering screen of length L, $\bar{n} \sim 0.99$. From Eqn. 2,

$$\frac{\delta n}{\bar{n}} = \frac{1}{2\bar{n}^2}\left(\frac{\nu_p}{\nu}\right)^2 \frac{\delta N}{N}. \quad (15)$$

At R$\sim$1.65 $R_\odot$, assuming a typical L$\sim$0.175 $R_\odot$ and δN/N$\sim$0.5%, the $\delta n/\bar{n}$ for a harmonic emission originating locally would be $\sim$ 0.1%. But the radiation would experience a $\delta n/\bar{n}$ of only $\sim$ 0.01% at the edge of the scattering screen, L distance away. As the wave propagates further out, density falls steadily making $(\nu_p/\nu)^2$ term much smaller and $\bar{n}$ far more closer to unity, making scattering effects negligible. Also, note that L is a derived quantity based on observed propagation effects and we find that this is quite small compared to many physical property variation scales. The $\delta n/\bar{n}$ variation and values discussed justifies the smallness of L. Overall the model framework seems quite self-consistent.

4.1.4. Possible non-scattering effects

The AM & K19 framework works primarily due to the fact that the observed emission is at the second harmonic, which has a n$\approx$0.86 at the generation site itself leading to a low value of L. This high refractive index also ensures that the effects of refraction and reflection on wave propagation will be negligible compared to scattering effects, in contrast to the case for fundamental plasma emission generated close to n$\approx$0 surface (e.g. Kuznetsov et al. 2020). However, ensuring the absence of non-scattering effects in the SPREDS data will boost the confidence in the modelling framework used.

The effects of refraction and reflection is usually manifested in the dynamic spectrum as drift-pair bursts (See, Melnik et al. 2005, for an overview). Drift-pair (DP) features appear as short-lived forward or reverse drifting parallel emission streaks imprinted on the type-III emission feature in the dynamic spectrum, with clearly distinguishable drift rates and brightness. With typical drift rates of $\approx$ 1 – 2 MHz/s, they last for $\approx$ 1 – 2 s. Though 0.5 s resolution can only barely separate any DPs in the time domain, the drift rates $\lesssim$ 2 MHz/s should make the pulse profiles close to the edges of the 2 MHz band different. But, the observed the pulse profiles are similar across every 2 MHz band as seen in the SPREDS (See, Fig. 2). Besides, DPs are reported only below 70 MHz so far. A long-term survey of these bursts by de La Noe & Moller Pedersen (1971), showed that 90% of the observed DPs fell in 20 – 45 MHz range. These events are found mostly associated with type-III storm events, where as the event in this work is a single isolated burst pulse.

4.2. Quantitative comparison with reported scattering effects

4.2.1. δN/N

Using methods based on remote sensing (Coles & Harmon 1989), the spectral fine structures in type-III bursts, the structural deformation of distant radio sources (Anantharamaiah et al. 1994) etc., δN/N had been estimated at different heights in the corona. Using Inter-Planetary Scintillation (IPS; Hewish 1955; Manoharan & Ananthakrishnan 1990, etc.) technique various groups had also estimated the strength of turbulence in the solar wind, which is beyond the scope of this comparative study.

Meanwhile, by modelling type-IIIb emission features, (Sharykin et al. 2018) and (Mugundhan et al. 2017) reported δN/N around 0.1 and 0.6% in the 30 – 80 MHz band, that explore a height range of $\approx$ 1.7 – 2.2 $R_\odot$. Mugundhan et al. (2017) also computed a power-law index, $\beta \approx 0.31 \pm 0.1$ for δN/N(R), which is quite different from my estimate in 80 – 140 MHz range. Recently, Chen et al. (2020) computed a mean stochastic fluctuation scale, $\overline{\kappa(\delta N/N)^2}$ by applying K19 model to type-III bust observations at 32 MHz. Using the reported value and assuming Eqn. 14, δN/N estimates to $\approx$0.6%. A caveat in the comparison of these results amongst each other and with that in 80 – 200 MHz band is the difference in the adopted models for coronal density

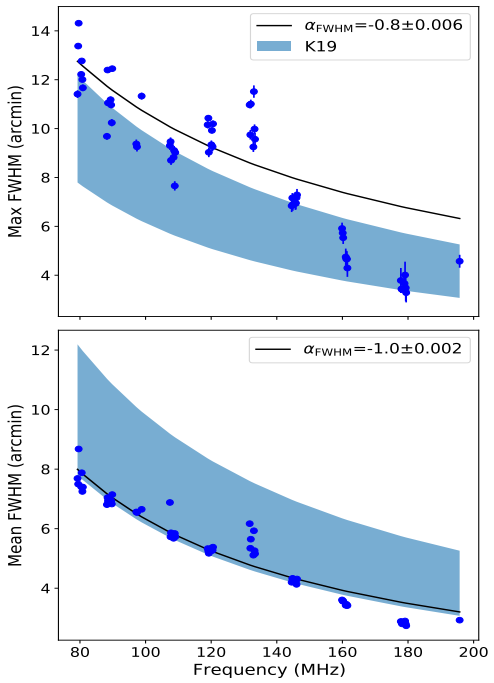

Fig. 6. The maximum and mean FWHM observed for the burst source across time at each observation frequency. Solid lines show the power-law fits to the data and the shaded region shows the expected range of source sizes based on K19 results.

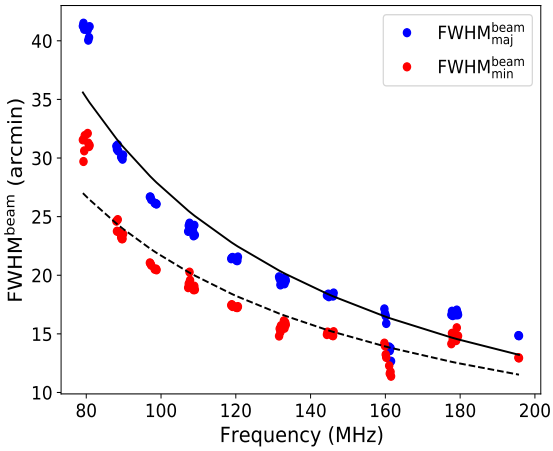

Fig. 7. The temporal mean FWHM of the synthesised beam along its major and minor axes. The solid and dashed lines show the best-fit power-law functions for $FWHM^{beam}_{maj}$ and $FWHM^{beam}_{min}$ respectively.

and characteristic spatial scales like l_o and l_i. However, despite these differences in the models and the techniques used, δN/N estimates over the wide range from 30 – 140 MHz (R ≈ 1.5 – 2.2$R_\odot$) agree within a few factors.

4.2.2. Scattered source size

Owing to sub-second time resolution of the data, an evolving source size is observed in this work during the type-III event. So, to compare the observed source sizes across frequency with the literature values, which mostly lack the time evolution information, the maximum and the mean FWHM of the source observed over time are considered, at each observation frequency. The FWHM is computed as $\sqrt{A_{obs}/\pi}$, where A_{obs} is the observed source area. A power-law fit was performed to both estimates of FWHM as a function of frequency and spectral indices (α_{FWHM}) were obtained. Fig. 6 shows the FWHM variation along with the spectral index α_{FWHM} for both mean (-1.0±0.002) and maximum (-0.8±0.006) values. The solid line curve shows the best-fit function obtained for the data. The shaded band labelled K19 shows the expected size range from the best-fit model derived by K19 using a compilation of archival estimates of source sizes. It can be seen that the observed mean source sizes falls roughly within the expected range, but the maximum values are tend to fall out especially at higher frequencies. However, if all area estimates across time are over-plotted for every frequency, they would populate the K19 predicted band with some values below and above the predicted range. The α_{FWHM} estimates for the mean and maximum area data flank the K19 value of 0.98±0.05.

Meanwhile, a significant spike in the observed area is noted at 130 MHz in both mean and maximum values. This is not an anomaly due to variations in the synthesised beam size, since the analysis uses beam-deconvolved source sizes. However, to discard the chances of any possible imaging-related systematic effects, the variation of the FWHM of the beam across its major and minor axes ($FWHM^{beam}_{maj(min)}$)was studied across time and frequency. It was found that the $FWHM^{beam}_{maj(min)}$ remained constant across time for any particular frequency. The temporal mean of the $FWHM^{beam}_{maj(min)}$ was estimated as a function of frequency. Fig. 7 shows the spectral variation of this mean $FWHM^{beam}_{maj(min)}$ along with the best-fit power-law models for the same (Solid line: $FWHM^{beam}_{maj}$; dashed line: $FWHM^{beam}_{min}$). The spectral indices for $FWHM^{beam}_{maj}$ and $FWHM^{beam}_{min}$ were found to be -1 and -0.95 respectively, consistent with the expected trend in angular resolution with frequency for a fixed array configuration. Also, no anomalous behaviour is seen in $FWHM^{beam}_{maj,min}$ near 130 MHz. So the observed spike in the deconvolved source sizes around 130 MHz is real. This frequency corresponds to the height around 1.65 – 1.7 $R_\odot$. The δN/N(R), which depends on the growth rate rather than on the absolute value of source area also showed a local spike in this height range. Both these observations suggest an enhanced turbulence in this narrow region.

4.2.3. Burst pulse decay time (τ_{decay})

The observed burst pulse profiles are well modelled by a Gaussian profile. Gaussian function gave better χ^2-fits than either the complete analytical profile function derived by AM (See, Eqn. 65 in AM), or its non-Gaussian limiting functional forms. Meanwhile, at frequencies above 130 MHz, a skewed burst profile start becoming evident. But since the burst pulses are only a few seconds wide with the rising and decay phases lasting barely for a second or two, it was impossible to get reliable χ^2-fits for separate exponential models in the two phases. So, Gaussian profiles were fit to burst pulses across all chosen observation frequencies. The half width at half maximum of the Gaussian pulse profile gave an estimate of the burst decay time, τ_{decay}, across frequencies. Fig. 8 shows $\tau_{decay}(\nu)$ with the best-fit power-law function with a α_τ, of -0.95±0.04 in solid line. Fitting a power-law to the archival estimates of τ_{decay} across frequency, K19 had found a similar spectral index of -0.97±0.3. Meanwhile, a comparison of the observed τ_{decay} values with the expected range from K19 model (shaded band in Fig. 8) shows that the absolute values of the observed τ_{decay} are higher than expected.

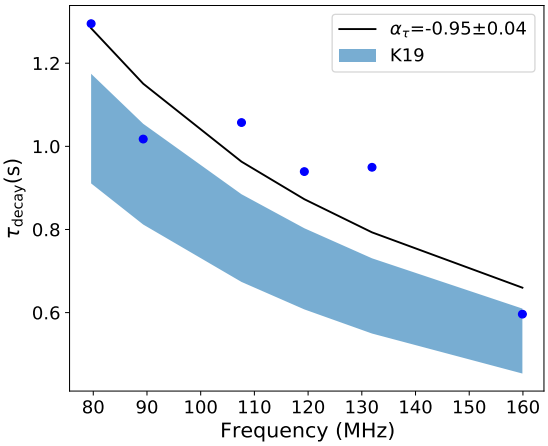

Fig. 8. Pulse decay time, τ_{decay} Vs frequency. Solid line shows the best-fit power-law function to the data with spectral index, α_τ. Shaded band represents the expected range of values from the K19 results.

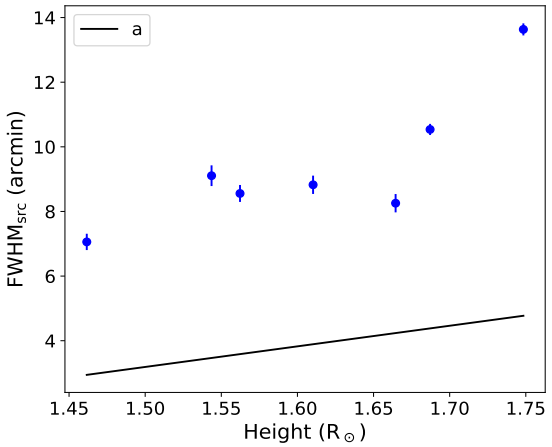

Fig. 9. The true source sizes (FWHM$_{src}$) Vs height after correcting for scatter broadening. Solid line shows the empirical model for the size (a) of coronal flux tubes.

4.3. The intrinsic source sizes

Since the δN/N values across the explored heights are well above the respective δN/N$_{sat}$ values, region of corona under study is in the strong turbulence regime. So the scatter broadening effect is expected to cause an area rise by an amount equal to the theoretical saturation area ($\pi\sigma_{sat}{}^2$). The intrinsic source sizes, σ_{src}, can hence be found from the observed source area, A_{obs} (Fig. 2) as follows,

$$\sigma_{src} = \sqrt{A_{obs}/\pi - \sigma_{sat}^2} \quad (16)$$

Since this equation will be valid only after the source area growth phase, I apply it to the maximum source sizes observed at each frequency. Fig. 9 shows the FWHM values for the intrinsic Gaussian burst source across height (FWHM$_{src}$). It is compared with the typical width of magnetic flux tubes (a) across height as per the empirical scaling relation (a≈0.4×[R-1]) proposed by Aschwanden (2003). Interestingly, the empirical estimates though were proposed for closed coronal loops, are similar to the derived intrinsic source sizes within an order of magnitude. The type-III bursts are expected to be associated with open coronal loops (Reid & Ratcliffe 2014), which are usually more wider than the closed loops at a given height.

5. Conclusion

I present a snapshot spectroscopic study of the evolution of a type-III burst at sub-MHz and sub-second resolution in 80 – 200 MHz band. The event was selected from the archival MWA Phase-I database such that it had a well discernible pulse profile and its source is close to the disk centre. These criteria ensured that the response of the corona to a burst pulse could be studied in both dynamic spectral and image plane without contamination from co-temporal and co-spatial events. The burst source had a 2D Gaussian structure at all times across frequency. So 2D Gaussian functions were fitted to the sources and the best-fit parameters were estimated after deconvolving the effect of the synthesised beam. The integrated flux density and area of the beam deconvolved source was studied across frequency and time.

The source area showed a linear rise simultaneous to that in flux density as expected from a diffusive propagation model of radiowaves across corona, subject to strong scattering. The area and integrated flux density profiles were modelled using the framework by Arzner & Magun (1999) and Kontar et al. (2019) to derive the strength of density fluctuations (δN/N) across height. The δN/N values ranged within 0.4 – 0.6% in the observation band. Combining with the earlier results in 30 – 80 MHz, it is found that the δN/N values agree within a few factors across 30 – 140 MHz (≈ 1.5 – 2.2R$_\odot$) despite the differences in the spatial profiles of coronal density and scattering scales assumed by various authors. The δN/N values roughly scaled with height (R) as $R^{2.2\pm0.73}$ in the range, R ≈ 1.54 – 1.75 R$_\odot$. The corona under study is found to be in a "strong turbulence regime". The scattering screen widths derived for the height range are significantly smaller than the outer scale of density fluctuations.

The FWHM of the Gaussian source Vs frequency was compared against the expected range from the fit derived by K19 using archival observations. It is found that the observed mean and maximum FWHM values roughly cover the expected range. However, the spectral index obtained for the mean and maximum FWHM of the source are -1.0±0.002 and -0.8±0.006, which flank the K19 value of -0.98±0.05. The source sizes showed a spike around 130 MHz, which correlated with an increased δN/N around 1.65 – 1.7 R$_\odot$.

The burst decay times (τ_{decay}) across frequency also showed a power-law with an index of -0.95±0.04. This is close to the estimate by K19, though the values of τ_{decay} lie outside the expected range from their model based on archival data.

Having estimated the effect of scatter broadening, I derive the intrinsic source sizes across R. The sizes increased with R and agreed with the empirical model for the closed flux tube widths proposed by Aschwanden (2003) within an order of magnitude.

Apart from the effect of scattering seen in the evolution of the burst source, I report an anti-phased pulsation with a time-lag of ≈ 2 – 3 s in the source area and integrated flux density. This could be attributed to a sausage-mode like motion at the particle acceleration/injection site which generated the type-III causing electron beams.

This work demonstrates the power of snapshot spectroscopic imaging across a wide spectral band to explore the evolution of coronal turbulence and derive its characteristics at coronal heights much closer to Sun than explored by Interplanetary scintillation (IPS) measurements. More of such works in different spectral bands are needed to understand the nature of solar coronal turbulence across a larger height range during different levels of solar activity.

Acknowledgements. We acknowledge the Wajarri Yamatji people as the traditional owners of the Observatory site. Support for the operation of the MWA is provided by the Australian Government's National Collaborative Research Infrastructure Strategy (NCRIS), under a contract to Curtin University administered by Astronomy Australia Limited. We acknowledge the Pawsey Supercomputing Centre, which is supported by the Western Australian and Australian Governments. This work is supported by the Research Council of Norway through its Centres of Excellence scheme, project number 262622 ("Rosseland Centre for Solar Physics"). AM acknowledges support from the EMISSA project funded by the Research Council of Norway (project number 286853). This research made use of NASA's Astrophysics Data System (ADS). AM is grateful to the developers of Python3 and various packages namely Numpy (Harris et al. 2020), Astropy (Astropy Collaboration et al. 2013), Scipy (Jones et al. 2001–) and Matplotlib (Hunter 2007).

References

Alcock, B. 2018, PhD thesis, , SPA, University of Galsgow, (2018)
Anantharamaiah, K. R., Gothoskar, P., & Cornwell, T. J. 1994, Journal of Astrophysics and Astronomy, 15, 387
Arzner, K. & Magun, A. 1999, A&A, 351, 1165
Aschwanden, M. J. 2003, ArXiv Astrophysics e-prints [astro-ph/0309505]
Aschwanden, M. J., Benz, A. O., Dennis, B. R., & Kundu, M. R. 1994, ApJS, 90, 631
Aschwanden, M. J., Nakariakov, V. M., & Melnikov, V. F. 2004, ApJ, 600, 458
Astropy Collaboration, Robitaille, T. P., Tollerud, E. J., et al. 2013, A&A, 558, A33
Chen, X., Kontar, E. P., Chrysaphi, N., et al. 2020, ApJ, 905, 43
Coles, W. A. & Harmon, J. K. 1989, ApJ, 337, 1023
de La Noe, J. & Moller Pedersen, B. 1971, A&A, 12, 371
Dulk, G. A., Steinberg, J. L., & Hoang, S. 1984, A&A, 141, 30
Ginzburg, V. L. & Zhelezniakov, V. V. 1958, Soviet Ast., 2, 653
Harris, C. R., Millman, K. J., van der Walt, S. J., et al. 2020, Nature, 585, 357
Hewish, A. 1955, Proceedings of the Royal Society of London Series A, 228, 238
Hunter, J. D. 2007, Computing in science & engineering, 9, 90
Jones, E., Oliphant, T., Peterson, P., et al. 2001–, SciPy: Open source scientific tools for Python
Kontar, E. P., Chen, X., Chrysaphi, N., et al. 2019, ApJ, 884, 122
Kontar, E. P., Yu, S., Kuznetsov, A. A., et al. 2017, Nature Communications, 8, 1515
Kuznetsov, A. A., Chrysaphi, N., Kontar, E. P., & Motorina, G. 2020, ApJ, 898, 94
Manoharan, P. K. & Ananthakrishnan, S. 1990, MNRAS, 244, 691
McMullin, J. P., Waters, B., Schiebel, D., Young, W., & Golap, K. 2007, in Astronomical Society of the Pacific Conference Series, Vol. 376, Astronomical Data Analysis Software and Systems XVI, ed. R. A. Shaw, F. Hill, & D. J. Bell, 127
Melnik, V. N., Konovalenko, A. A., Dorovskyy, V. V., et al. 2005, Sol. Phys., 231, 143
Melrose, D. B. & Sy, W. N. 1972, Australian Journal of Physics, 25, 387
Mohan, A. 2021, ApJ, 909, L1
Mohan, A., Mondal, S., Oberoi, D., & Lonsdale, C. J. 2019, ApJ, 875, 98
Mohan, A. & Oberoi, D. 2017, Sol. Phys., 292, 168
Mondal, S., Mohan, A., Oberoi, D., et al. 2018, Proceedings of the International Astronomical Union, 13, 159–160
Mondal, S. & Oberoi, D. 2021, ApJ, 920, 11
Mugundhan, V., Hariharan, K., & Ramesh, R. 2017, Sol. Phys., 292, 155
Rahman, M. M., McCauley, P. I., & Cairns, I. H. 2019, Sol. Phys., 294, 7
Reid, H. A. S. & Ratcliffe, H. 2014, Research in Astronomy and Astrophysics, 14, 773
Robinson, P. A. & Cairns, I. H. 1994, Sol. Phys., 154, 335
Robinson, R. D. 1983, Proceedings of the Astronomical Society of Australia, 5, 208
Rosenberg, H. 1970, A&A, 9, 159
Sasikumar Raja, K., Subramanian, P., Ramesh, R., Vourlidas, A., & Ingale, M. 2017, ApJ, 850, 129
Sharykin, I. N., Kontar, E. P., & Kuznetsov, A. A. 2018, Sol. Phys., 293, 115
Steinberg, J. L., Aubier-Giraud, M., Leblanc, Y., & Boischot, A. 1971, A&A, 10, 362
Tingay, S. J., Goeke, R., Bowman, J. D., et al. 2013, PASA, 30, e007
Tsytovich, V. N. & Kaplan, S. A. 1969, Soviet Ast., 12, 618
van Haarlem, M. P., Wise, M. W., Gunst, A. W., et al. 2013, A&A, 556, A2
Wang, M., Duan, C. C., Xie, R. X., & Yan, Y. H. 2003, Sol. Phys., 212, 401
Wayth, R. B., Tingay, S. J., Trott, C. M., et al. 2018, PASA, 35, 33
Wild, J. P. 1950, Australian Journal of Scientific Research A Physical Sciences, 3, 541
Wohlmuth, R., Plettemeier, D., Edenhofer, P., et al. 2001, Space Sci. Rev., 97, 9
Zhang, P., Wang, C., & Kontar, E. P. 2021, ApJ, 909, 195